

# Improved Na-storage cycling of amorphous-carbon-sheathed Ni<sub>3</sub>S<sub>2</sub> arrays and investigation by in situ TEM characterization



Xueke Xia<sup>a,1</sup>, Qiannan Wang<sup>a,b,1</sup>, Qi Zhu<sup>a,b,1</sup>, Jian Xie<sup>a,c,\*</sup>, Jiangwei Wang<sup>a,b,\*\*</sup>,  
Dagao Zhuang<sup>d</sup>, Shichao Zhang<sup>e</sup>, Gaoshao Cao<sup>a</sup>, Xinbing Zhao<sup>a,c</sup>

<sup>a</sup> State Key Laboratory of Silicon Materials and School of Materials Science and Engineering, Zhejiang University, Hangzhou 310027, China

<sup>b</sup> Center of Electron Microscopy and School of Materials Science and Engineering, Zhejiang University, Hangzhou 310027, China

<sup>c</sup> Key Laboratory of Advanced Materials and Applications for Batteries of Zhejiang Province, Hangzhou 310027, China

<sup>d</sup> Dynabatt New Energy Science & Technology Co., Ltd., Zhaoan 363500, China

<sup>e</sup> School of Materials Science and Engineering, Beijing University of Aeronautics and Astronautics, Beijing 100191, China

## ARTICLE INFO

### Article history:

Received 9 March 2017

Received in revised form

26 April 2017

Accepted 14 May 2017

### Keywords:

Nickel sulfide

Amorphous carbon sheath

Array electrode

Sodium ion battery

In situ transmission electron microscopy

## ABSTRACT

The past few years have witnessed increasing attention of sodium ion batteries due to the concerns on the shortage of lithium resources. Great challenge, however, remains to develop anode materials with high capacity and long cycle life. In this work, a binder-free array-type electrode, constructed of nickel sulfide (Ni<sub>3</sub>S<sub>2</sub>) nanoparticles encapsulated in amorphous carbon sheath (ACS), was fabricated by a facile templating method. This array-type Ni<sub>3</sub>S<sub>2</sub>/ACS electrode can yield a high initial reversible capacity of 772 mAh g<sup>-1</sup> and a long cycle life with a reversible capacity of 440 mAh g<sup>-1</sup> retained after 100 cycles. Both ex situ and in situ characterizations reveal that the excellent electrochemical performance of Ni<sub>3</sub>S<sub>2</sub>/ACS electrode originates from the unique array-type structure, in which high activity of Ni<sub>3</sub>S<sub>2</sub> can be obtained by the thin-layered structure and the sodiation-induced volume expansion of Ni<sub>3</sub>S<sub>2</sub> can be effectively accommodated by the carbon sheath and inner space, resulting in a high mechanical stability of the Ni<sub>3</sub>S<sub>2</sub>/ACS rods during cycling. Our results reveal the electrochemical performance and fundamental reaction mechanism of Ni<sub>3</sub>S<sub>2</sub>/ACS during sodiation-desodiation cycles, shedding lights onto the design of novel sulfide-based anodes for sodium ion batteries.

© 2017 Elsevier Ltd. All rights reserved.

## 1. Introduction

Modern society has witnessed the ever increasing applications of Li-ion batteries (LIBs) in portable electronic devices (e.g. smart phone, laptop, and digital camera) and electric vehicles (EV), to reduce the dependence on fossil fuels and greenhouse gas emission [1–4]. The shortage of lithium reserves and currently immature battery recycling technology, however, cause a serious concern about the sustainable application of LIBs in near future [5–7]. As a consequence, batteries based on the alkali metals with abundant resources and low costs, such as Na-ion batteries (NIBs), have

grained more and more attentions during past few years [6–12]. NIBs show potential applications in electrical energy storage for grid, solar cells and wind turbines, where the energy density is not a concern [11,13,14]. A critical problem of NIBs is the low electrochemical activity compared with LIBs [15], which is ascribed to the large radius of sodium ions, resulting in its difficulty to insert into the intercalation-type anodes, such as the widely-used graphitized carbon materials in commercial LIBs [16,17]. Inspired by the knowledge of LIBs, alloying and conversion type electrodes may be a potential solution to overcome this challenge in NIBs. For the alloying mechanism, recent studies have showed that sodium can reversibly alloy/dealloy with some metals and alloys (e.g. Sb, Sn, hollow NiSb and Sn-P-based composite, etc) to deliver high capacity and good cycling stability [18–27].

Among the conversion-type anodes, previous studies mainly focused on the transition metal oxides [25,27], which delivered high Na-storage capacity but still suffered from low Na-storage activity. Recently, sulfides, such as FeS<sub>2</sub> [28], FeS [29], CoS<sub>2</sub> [30], Co<sub>9</sub>S<sub>8</sub> [31], MoS<sub>2</sub> [32–34], WS<sub>2</sub> [35,36], and Ni<sub>3</sub>S<sub>2</sub> [37,38], were

\* Corresponding author. School of Materials Science and Engineering, Zhejiang University, Hangzhou 310027, China.

\*\* Corresponding author. School of Materials Science and Engineering, Zhejiang University, Hangzhou 310027, China.

E-mail addresses: xiejian1977@zju.edu.cn (J. Xie), jiangwei\_wang@zju.edu.cn (J. Wang).

<sup>1</sup> Xueke Xia, Qiannan Wang, and Qi Zhu contributed equally to this work.

found to demonstrate high Na-storage activities, along with other advantages including low cost, environmental friendliness and easy preparation. Nevertheless, rapid capacity fade often occurred during the application of these conversion-type sulfide anodes in NIBs owing to the large volume changes upon sodiation/desodiation. Further engineering the sulfides with flexible matrix, such as graphene nanosheets (GNS) and carbon nanofibers (CNF), were further employed to alleviate the electrochemical degradation and thereby capacity fade of sulfide anodes [39,40]. For example, a MoS<sub>2</sub>/GNS hybrid could deliver an initial capacity of 573 mAh g<sup>-1</sup> at 200 mA g<sup>-1</sup> and maintain a capacity of 322 mAh g<sup>-1</sup> after 600 cycles at 1.3 A g<sup>-1</sup> [33]; while the Sb nanoparticles encapsulated in macroporous carbon could keep 93% of its initial capacity after 500 cycles [41]. As a typical sulfide, the electrochemical performance of Ni<sub>3</sub>S<sub>2</sub> anode in NIBs, however, remains unsatisfactory yet [37,38,42].

In this work, we designed a binder-free array-type electrode by a simple templating method. In this electrode, Ni<sub>3</sub>S<sub>2</sub> were directly grew and encapsulated inside amorphous carbon sheath (ACS), forming three-dimensional (3D) hollow-structural Ni<sub>3</sub>S<sub>2</sub>/ACS arrays on Ni foam substrate. In situ transmission electron microscopy (TEM) electrochemical testing revealed that the volume expansion of Ni<sub>3</sub>S<sub>2</sub> during the sodiation process can be effectively buffered by the voids inside the ACS, and the structural integrity of the Ni<sub>3</sub>S<sub>2</sub>/ACS rods can be kept by the carbon sheath after electrochemical cycling. As a result, the Ni<sub>3</sub>S<sub>2</sub>/ACS arrays exhibited a high initial capacity of 722 mAh g<sup>-1</sup> at 50 mA g<sup>-1</sup> and a long cycle life with a capacity of 440 mAh g<sup>-1</sup> retained after 100 cycles.

## 2. Experimental section

### 2.1. Preparation of ZnO nanorods (NRs) on Ni substrate

The ZnO NRs were synthesized on Ni substrate by a facile hydrothermal route. In a typical synthesis, Zn(NO<sub>3</sub>)<sub>2</sub>·6H<sub>2</sub>O (268 mg) and methenamine (127 mg) were dissolved in 30 mL of deionized (DI) water with magnetic stirring for 10 min to form a uniform solution. Then, 2.4 mL of ammonia water (25 wt%) was added to the above solution with stirring for 15 min to obtain a transparent solution. A piece of Ni foam (1.6 cm × 4.8 cm) was immersed in a KMnO<sub>4</sub> aqueous solution (0.5 mol L<sup>-1</sup>) for 1 h and rinsed with DI water sufficiently, which was then steeped in the above transparent solution for 10 h. After that, the solution with Ni foam was transferred into a 50 mL Teflon-lined stainless steel autoclave and held at 90 °C for 24 h in an electric oven before cooling down to room temperature. The Ni-supported ZnO was finally obtained by rinsing with DI water and absolute ethanol several times followed by heating at 60 °C in air overnight.

### 2.2. Preparation of Ni-supported Ni<sub>3</sub>S<sub>2</sub>/ACS

The Ni-supported ZnO NRs were used as templates to grow Ni-supported Ni<sub>3</sub>S<sub>2</sub>/ACS. First, a solution for Ni<sub>3</sub>S<sub>2</sub> growth was prepared by mixing 30 mg of thioacetamide and 142 mg of Na<sub>2</sub>SO<sub>4</sub> in 35 mL of DI water under stirring for 30 min. The solution was then transferred into a 50 mL Teflon-lined stainless steel autoclave with the Ni-supported ZnO immersed. The autoclave was heated in an electric oven at 120 °C for 3 h followed by cooling to room temperature. The Ni foam with deposit was collected from the autoclave, washed with DI water and absolute ethanol several times, and heated at 60 °C in air overnight to obtain Ni-supported ZnO/Ni<sub>3</sub>S<sub>2</sub>. Carbon coating on ZnO/Ni<sub>3</sub>S<sub>2</sub> was conducted by immersing the Ni-supported ZnO/Ni<sub>3</sub>S<sub>2</sub> in an aqueous solution of glucose (0.06 mol L<sup>-1</sup>) overnight followed by firing at 500 °C in Ar for 3 h. The final product, Ni-supported Ni<sub>3</sub>S<sub>2</sub>/ACS was obtained by

immersing the above product in an aqueous solution of NaOH (1.5 mol L<sup>-1</sup>) for 48 h to remove ZnO. The preparation procedure of the Ni-supported Ni<sub>3</sub>S<sub>2</sub>/ACS is schematically illustrated in Fig. 1a. The electronic conductivity of the pyrolytic carbon from glucose and graphite was measured on a custom designed apparatus using a DC four-probe method.

### 2.3. Structural characterization

X-ray diffraction (XRD) patterns of the electrodes were collected on a Rigaku D/Max-2550pc powder diffractometer equipped with monochromatized Cu K<sub>α</sub> radiation (λ = 1.541 Å). Morphologies of the original and cycled electrodes were characterized by field-emission scanning electron microscopy (SEM) on an S-4800 microscope (Hitachi, Japan). The microstructures of the materials from the pristine and sodiated/desodiated electrodes were analyzed by TEM and High-resolution TEM (HRTEM) on a JEM 2100F microscope. For the post-mortem SEM and TEM characterizations, the electrodes or electrode components were carefully handled to minimize the exposure to air according to our previous report [43].

### 2.4. Electrochemical measurements

CR2025 coin cells were fabricated in an Ar-filled glove box with Na foils as counter electrodes, Ni<sub>3</sub>S<sub>2</sub>/ACS arrays on Ni substrate as working electrodes, and glass fiber (Whatman GF/D) as separators. Before cells fabrication, the working electrodes were dried at 110 °C in vacuum overnight. The electrolyte used was 1 M NaPF<sub>6</sub> in ethylene carbonate (EC)/diethyl carbonate (DEC) (1:1 in volume). Fluoroethylene carbonate (FEC) was used as electrolyte additive with a FEC/EC + DEC volume ratio of 5%. Cyclic voltammetry (CV) scanning was carried out on a VersaSTAT3 electrochemistry workstation (Princeton Applied Research) over a voltage range of 0.005–3 V (vs. Na/Na<sup>+</sup>) at 0.1 mV s<sup>-1</sup>. Galvanostatic cycling was conducted on a Neware battery cycler (Shenzhen, China) between 0.005 and 3.0 V (vs. Na/Na<sup>+</sup>) at various current densities. All of the electrochemical measurements were performed at 25 °C.

### 2.5. In situ TEM characterization

In situ TEM characterization was performed on a FEI Tecnai F20 TEM using the Nanofactory TEM-scanning tunneling microscopy (STM) holder. The configuration of the device for in situ characterization is shown in Fig. S1. Typically, a nanosized Na cell was assembled to study the sodiation/desodiation mechanisms of Ni<sub>3</sub>S<sub>2</sub>/ACS electrodes. The nanosized NIB cell consisted of a working electrode of Ni<sub>3</sub>S<sub>2</sub>/ACS nanorods on a Pt rod, a counter electrode of metallic sodium on a W rod, and a solid electrolyte of Na<sub>2</sub>O + NaOH formed naturally on the surface of Na metal [44,45]. After the contact between solid electrolyte and Ni<sub>3</sub>S<sub>2</sub>/ACS was established, a potential of -1 V was applied to the Ni<sub>3</sub>S<sub>2</sub>/ACS to initiate the sodiation and +6–8 V for the desodiation. Both beam-on and beam-off experiments were carried out to exclude the beam irradiation on the alloying/dealloying processes.

## 3. Results and discussion

Fig. 1a shows the preparation procedure of Ni-supported Ni<sub>3</sub>S<sub>2</sub>/ACS arrays using Ni-supported ZnO NRs as the templates. In the as-fabricated products, Ni<sub>3</sub>S<sub>2</sub> is expected to be encapsulated in the carbon sheath. Fig. 1b and c show that ZnO NRs obtained by the hydrothermal reaction had a length of around 2–4 μm and were uniformly distributed on the skeleton of Ni foam substrate (Ni + ZnO). The porous structure of Ni foam was maintained, favoring the electrolyte wetting of electrode. After Ni<sub>3</sub>S<sub>2</sub> deposition,

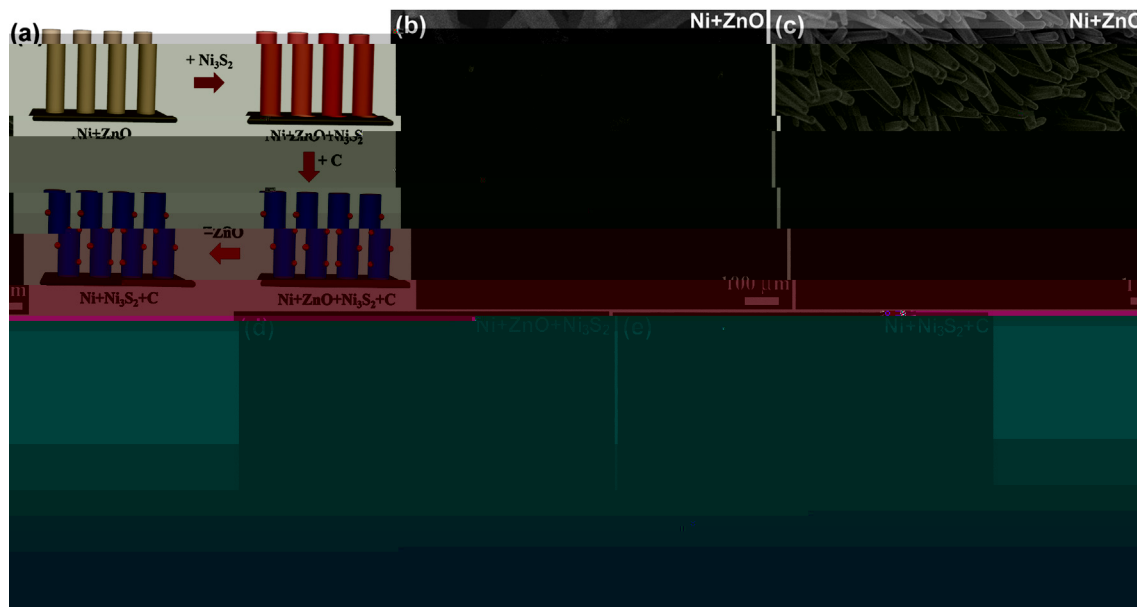


**Fig. 1.** (a) Schematic illustration of the synthetic route and (b–e) SEM images of the products at different synthetic stages.

no obvious morphology change occurred, indicating a conformal growth of  $\text{Ni}_3\text{S}_2$  on the surface of ZnO NRs (Ni + ZnO +  $\text{Ni}_3\text{S}_2$ , Fig. 1d). Ni-supported  $\text{Ni}_3\text{S}_2/\text{ACS}$  (Ni +  $\text{Ni}_3\text{S}_2+\text{C}$ ) arrays were then obtained by depositing carbon on Ni + ZnO +  $\text{Ni}_3\text{S}_2$  and subsequently removing ZnO NRs with NaOH etching, during which the array-type structure was well preserved but the surface roughness of  $\text{Ni}_3\text{S}_2/\text{ACS}$  arrays increased greatly compared with the pristine ZnO NRs (Fig. 1e). XRD patterns in Fig. 2 verify the successive formations of ZnO and  $\text{Ni}_3\text{S}_2$  during the fabrication of Ni-supported  $\text{Ni}_3\text{S}_2/\text{ACS}$ . No ZnO peak existed in the final products of Ni +  $\text{Ni}_3\text{S}_2+\text{C}$ , indicating the complete removal of ZnO after the etching. Raman spectrum in Supporting Information Fig. S2 confirms the presence of carbon in the final products, but it should be

in the amorphous state due to the lack of crystalline carbon peaks in the XRD diffraction of Ni +  $\text{Ni}_3\text{S}_2+\text{C}$ .

TEM analysis was further conducted to characterize the microstructure of  $\text{Ni}_3\text{S}_2/\text{ACS}$  rods. Fig. 3a shows that the wall of each  $\text{Ni}_3\text{S}_2/\text{ACS}$  rod has a bilayer structure, with the thicknesses of 40–60 and 30–40 nm for the outer (light contrast) and inner layers (dark contrast), respectively, as demonstrated by the magnified view in Fig. 3b. According to the preparation procedure, the outer and inner layers of the wall should be carbon and  $\text{Ni}_3\text{S}_2$ , respectively, as verified by the high-angle annular dark-field (HAADF)-scanning transmission electron microscopy (STEM) images and the corresponding energy dispersive X-ray spectrometry (EDX) mapping in Fig. 3c–j. Clearly, the  $\text{Ni}_3\text{S}_2/\text{ACS}$  anode has a bilayer structure with the inner layer of  $\text{Ni}_3\text{S}_2$  and the outer layer of amorphous carbon (Fig. 3c–j). It is noted that the Ni and S elements also showed up in the carbon layer, as indicated by the superimposed EDS mapping in Fig. 3h–j. This should be induced by the diffusion of Ni and S during the pyrolysis treatment under high temperature, resulting in numerous  $\text{Ni}_3\text{S}_2$  nanoparticles on the surface of carbon layer, as demonstrated by Fig. S3.

Electrochemical sodiation/desodiation mechanism of the Ni-supported  $\text{Ni}_3\text{S}_2/\text{ACS}$  was investigated by CV scanning. Fig. 4a presents the first five cycles of CV plots swept at  $0.1 \text{ mV s}^{-1}$  in the voltage window of 0.005 and 3.0 V. During the first scan, there is a sharp reduction peak between 0 and 0.5 V, which can be attributed to the electrolyte decomposition reaction and the conversion reaction  $4\text{Na}^+ + 4\text{e}^- + \text{Ni}_3\text{S}_2 \rightarrow 3\text{Ni} + 2\text{Na}_2\text{S}$  [37]. In the second scan, two reduction peaks appear between 0.5 and 1.0 V, suggesting different reactions occurred as compared with the first cycle. In the first anodic scan, the sharp peak at around 2.0 V is assigned to the decomposition of  $\text{Na}_2\text{S}$  ( $\text{Na}_2\text{S} \rightarrow \text{S} + 2\text{Na}^+ + 2\text{e}^-$ ). During the subsequent scans, the anodic peaks are almost overlapped, indicative reversible reactions. However, it is yet unclear that whether the  $\text{Ni}_3\text{S}_2$  crystal lattice can be recovered after charge, which will be clarified by the in situ TEM characterization as discussed below. The electrochemical Na-storage performance of the Ni-supported  $\text{Ni}_3\text{S}_2/\text{ACS}$  was evaluated by galvanostatic cycling at  $50 \text{ mA g}^{-1}$  between 0.005 and 3.0 V, with the initial three charge/discharge cycles shown in Fig. 4b. The electrode delivers the first discharge

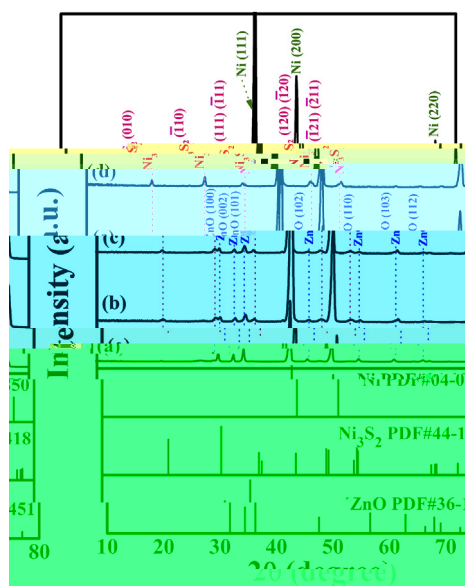


**Fig. 2.** XRD patterns of the products at different synthetic stages with final product Ni-supported  $\text{Ni}_3\text{S}_2/\text{ACS}$ : (a) Ni + ZnO, (b) Ni + ZnO +  $\text{Ni}_3\text{S}_2$ , (c) Ni + ZnO +  $\text{Ni}_3\text{S}_2+\text{C}$ , and (d) Ni +  $\text{Ni}_3\text{S}_2+\text{C}$ .

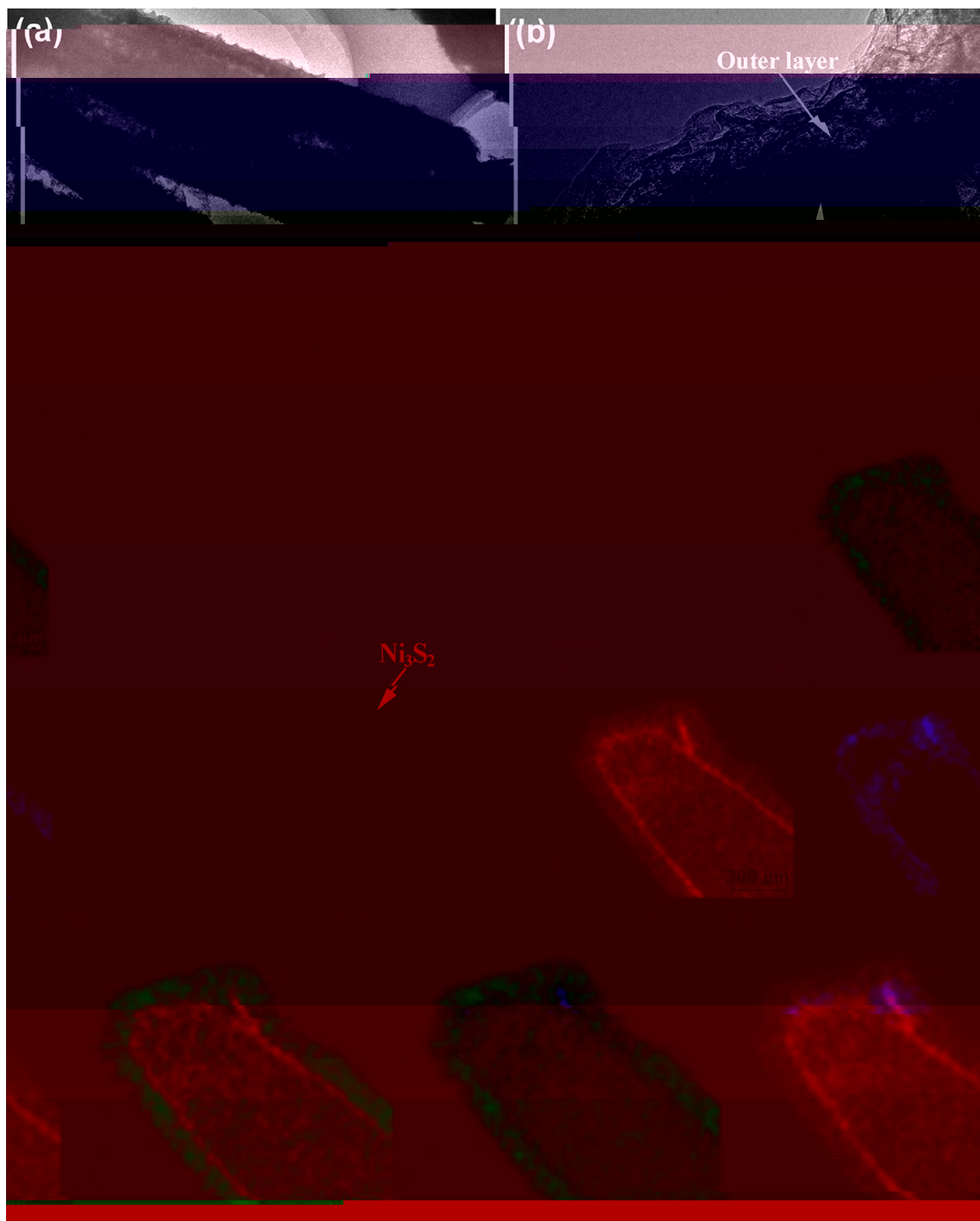


**Fig. 3.** (a, b) TEM images, (c–g) HAADF-STEM image and EDS mapping of  $\text{Ni}_3\text{S}_2/\text{ACS}$ , and (h–j) superimposed EDS mapping.

(sodiation) and charge (desodiation) capacities of  $1193$  and  $772 \text{ mAh g}^{-1}$ , respectively, which are higher than those in the previous reports [37,38,42]. The higher electrochemical activity of  $\text{Ni}_3\text{S}_2/\text{ACS}$  may be due to such factors as array-type structure that facilitates electrode wetting, small size of the  $\text{Ni}_3\text{S}_2$  particles and good contact between amorphous carbon and  $\text{Ni}_3\text{S}_2$ . Fig. 4c shows the cycling performance of the Ni-supported  $\text{Ni}_3\text{S}_2/\text{ACS}$  electrode at  $50 \text{ mA g}^{-1}$ . It can be seen that the electrode shows relatively stable cycling after initial relatively rapid capacity fade. After 100 cycles,  $\text{Ni}_3\text{S}_2/\text{ACS}$  can maintain a high charge capacity of  $440 \text{ mAh g}^{-1}$ ,

which is higher than those of the carbon-based materials [16]. The electronic conductivity of the carbon pyrolyzed from glucose at  $1000^\circ\text{C}$  is only  $0.26 \text{ S cm}^{-1}$  at room temperature, much lower than that of the graphite ( $210 \text{ S cm}^{-1}$  at room temperature). Therefore, ACS may only act as the substrate to support  $\text{Ni}_3\text{S}_2$  after ZnO etching and contributes little to the improvement of the electronic conductivity. Actually, the rate performance of  $\text{Ni}_3\text{S}_2/\text{ACS}$  electrode is not satisfactory (Fig. S4a). We compared the electrochemical performance between  $\text{Ni}_3\text{S}_2/\text{ACS}$  arrays and the  $\text{Ni}_3\text{S}_2$  particles grown directly on Ni foam. It can be seen that with the supporting and

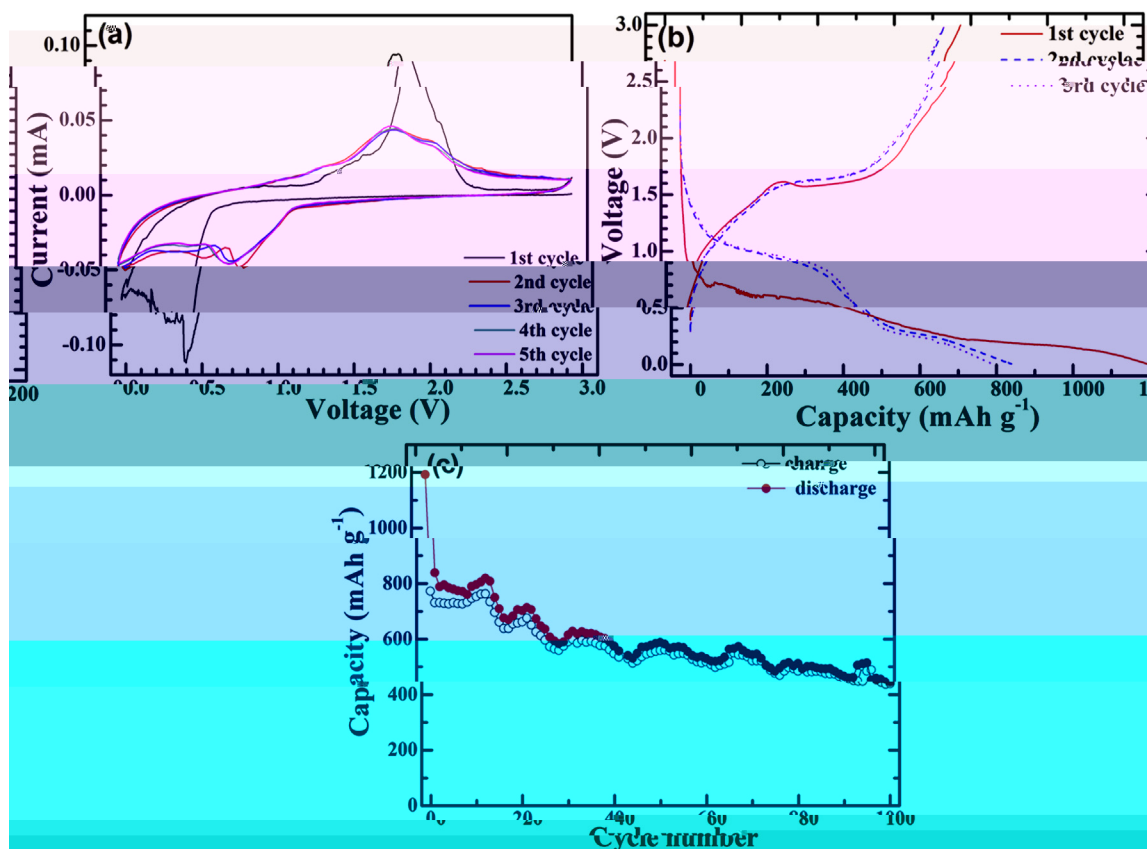


Fig. 4. (a) CV plots, (b) voltage profiles and (c) cycling stability of  $\text{Ni}_3\text{S}_2/\text{ACS}$  at  $50 \text{ mA g}^{-1}$ .

dispersing effect of ACS, the  $\text{Ni}_3\text{S}_2/\text{ACS}$  shows a higher reversible capacity and improved cycling performance (Fig. S4b).

Ex-situ and in situ characterizations were conducted to understand the good cycling stability of  $\text{Ni}_3\text{S}_2/\text{ACS}$ . SEM image in Fig. 5a shows that the array-type structure of Ni-supported  $\text{Ni}_3\text{S}_2/\text{ACS}$  electrode is well kept after discharge, indicating its mechanical robustness during cycling; however, the surface roughness of the discharged rods increases significantly due to the formation of solid electrolyte interface (SEI) layers on the outer surface. TEM image in Fig. 5b displays that the bilayer structure of  $\text{Ni}_3\text{S}_2/\text{ACS}$  is well preserved and the  $\text{Ni}_3\text{S}_2$  remains confined inside the carbon sheath after sodiation, suggesting the robust behavior of the  $\text{Ni}_3\text{S}_2/\text{ACS}$  array upon the reversible volume changes. Selected area electron diffraction (SAED) pattern in Fig. 5c shows that the sodiation product is  $\text{Na}_2\text{S}$  and Ni, consistent with the CV measurement. The SAED pattern also indicates that there is residual  $\text{Ni}_3\text{S}_2$  in the sodiation product. After desodiation, no fracture or pulverization occurs in this array-type  $\text{Ni}_3\text{S}_2/\text{ACS}$  after reversible volume changes (Fig. 5d).

Movies have been captured to show the dynamic structural changes of  $\text{Ni}_3\text{S}_2/\text{ACS}$ . Fig. 6 and Movie S1 present the dynamic structural changes of an individual  $\text{Ni}_3\text{S}_2/\text{ACS}$  anode upon sodiation and desodiation. The pristine  $\text{Ni}_3\text{S}_2/\text{ACS}$  rod consists of the inner layer of  $\text{Ni}_3\text{S}_2$  (dark contrast) and the outer layer of carbon (light contrast), with a taper structure along the axial direction. A small  $\text{Ni}_3\text{S}_2$  nanoparticle (with the diameter of 180 nm) is attached onto the surface of this  $\text{Ni}_3\text{S}_2/\text{ACS}$  rod (pointed out by the black arrow in Fig. 6a), enabling a direction comparison between the sodiation/desodiation behavior of bare  $\text{Ni}_3\text{S}_2$  and  $\text{Ni}_3\text{S}_2/\text{ACS}$  anodes. Fig. 6a–f demonstrate that this  $\text{Ni}_3\text{S}_2/\text{ACS}$  rod shows a robust behavior in one sodiation/desodiation cycle, consistent with the ex situ observation

presented in Fig. 5. Upon sodiation, we observe that the volume expansion of the inner  $\text{Ni}_3\text{S}_2$  layer can be completely accommodated by the amorphous carbon without any structural damage due to the mechanical confinement and buffering effect of surface carbon layer [46], though the sodiation-induced diameter increase of  $\text{Ni}_3\text{S}_2/\text{ACS}$  rod still occurs because of the sodiation-induced large hoop strains that results in outward radial displacement [46]. After full reaction, the diameter of this  $\text{Ni}_3\text{S}_2/\text{ACS}$  rod increases from 751 nm to 815 nm with negligible axial elongation, corresponding to a radial expansion of  $\sim 8.5\%$  (Due to overlapping with the other sample, the changes of inner diameter of this  $\text{Ni}_3\text{S}_2/\text{ACS}$  rod cannot be clearly identified). In strong contrast, without the protection of carbon coating, a large crack appears on the bare  $\text{Ni}_3\text{S}_2$  nanoparticle upon the initial sodiation (pointed out by the red arrow in Fig. 6b). Such sodiation-induced crack could result in the pulverization and thereby capacity fading of pure  $\text{Ni}_3\text{S}_2$  anode. It should be mentioned that a large particle with the diameter of 500 nm is formed the surface of ACS sheath after 70 s sodiation (pointed out by the black arrow in Fig. 6c), which is the Na dendrite nucleated during sodiation via the fast surface diffusion under the high potential. Similar phenomenon was observed in other in situ TEM studies of other anodes for sodium-ion batteries, such as Sn nanoparticle [47], which should be avoided in real batteries. After full sodiation, the pristine  $\text{Ni}_3\text{S}_2$  phase is transformed to  $\text{Na}_2\text{S}$  and Ni phases (identified by the SAED patterns in Fig. 6g and h), confirming the conversion reaction of  $4\text{Na}^+ + 4\text{e}^- + \text{Ni}_3\text{S}_2 \rightarrow 3\text{Ni} + 2\text{Na}_2\text{S}$  [37]. Note that some sodium dendrites also form on the surface of sodiated sample due to the overcharge (pointed out by the black arrow in Fig. 6c), which will shrink and eventually disappear with the extraction of sodium ions. In the following desodiation, the sodiation product of  $\text{Na}_2\text{S}$  is gradually transformed

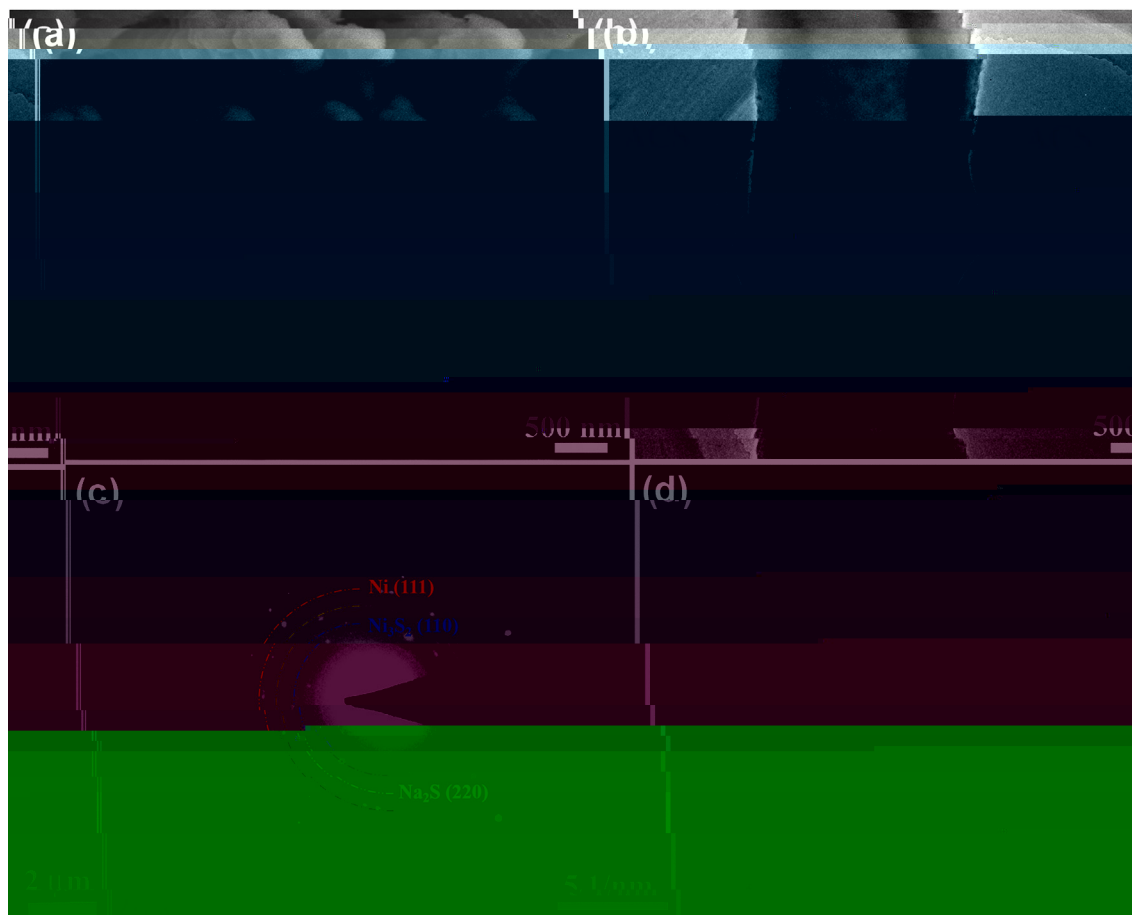
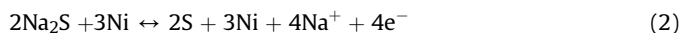
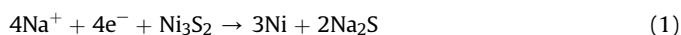


Fig. 5. (a) SEM image, (b) TEM image and SAED patterns of  $\text{Ni}_3\text{S}_2/\text{ACS}$  after the first discharge, and (d) SEM image of  $\text{Ni}_3\text{S}_2/\text{ACS}$  after the first charge.

back to S, causing diameter shrinkage of the sodiated rod (Fig. 6d–f and Movie S2). SAED pattern in Fig. 6i indicates that the desodiation products are S and Ni, suggesting that the recovery of the  $\text{Ni}_3\text{S}_2$  lattice cannot be achieved. In other words, the capacity comes from the reversible sodiation/desodiation of element S in Ni matrix. The total reaction mechanism can be written as:



The reaction mechanism of the  $\text{Ni}_3\text{S}_2/\text{ACS}$  arrays is also schematically illustrated in Fig. S5.

Supplementary video related to this article can be found at <http://dx.doi.org/10.1016/j.mtener.2017.05.003>.

Fig. 7 and Movie S3 show the sodiation of another  $\text{Ni}_3\text{S}_2/\text{ACS}$  rod, in which the dynamic changes of the inner diameter can be clearly identified. Similar to the sample shown in Fig. 6, sodiation causes an outward expansion of the  $\text{Ni}_3\text{S}_2/\text{ACS}$  rod, with a radial expansion of 13.5% after full sodiation. More importantly, the sodiation also results in a decrease of the inner diameter from 524 nm to 495 nm, which can be attributed to the mechanical confinement of surface carbon layers on the inner  $\text{Ni}_3\text{S}_2$  layer. Such inward expansion, to some extent, could alleviate the outward expansion-induced pulverization and thereby fracture of SEI layer formed on the outer surface of  $\text{Ni}_3\text{S}_2/\text{ACS}$  rod. As a result, high mechanical stability is obtained in our Ni-supported array-type  $\text{Ni}_3\text{S}_2/\text{ACS}$  electrode structure. However, it should be stated that the array-type  $\text{Ni}_3\text{S}_2/\text{ACS}$

electrode still shows capacity fade despite the robust structure of the  $\text{Ni}_3\text{S}_2/\text{ACS}$  rods. This may be caused by the dissolution of the polysulfides during cycling, similar to the case in Li–S batteries [48]. As shown in Fig. S6, numerous small particles form on the surface of sodiated  $\text{Ni}_3\text{S}_2/\text{ACS}$  rod, which are reaction products of surface  $\text{Ni}_3\text{S}_2$  particles, i.e.  $\text{Na}_2\text{S}$  and Ni nanoparticles. In the subsequent cycling, their desodiation product of S can be dissolved into the electrolytes in real batteries, causing gradual capacity decay. Therefore, further work need to be conducted for optimizing the structure design of array-type  $\text{Ni}_3\text{S}_2/\text{ACS}$  electrodes to achieve an improved battery performance.

#### 4. Conclusions

In summary, a binder-free array-type  $\text{Ni}_3\text{S}_2/\text{ACS}$  electrode was fabricated directly on Ni foam substrate by a facile route using ZnO NRs as the templates. The small size and intimate contact with amorphous carbon endow  $\text{Ni}_3\text{S}_2$  with a high electrochemical Na-storage activity. The  $\text{Ni}_3\text{S}_2/\text{ACS}$  array electrode can deliver a high reversible capacity of  $772 \text{ mAh g}^{-1}$  at a current density of  $50 \text{ mA g}^{-1}$ . The volume expansion of  $\text{Ni}_3\text{S}_2$  upon sodiation can be buffered by the carbon sheaths and inner space, leading to the structural robustness of the array-type electrode. As a result, the  $\text{Ni}_3\text{S}_2/\text{ACS}$  array electrode exhibits a long cycle life with a reversible capacity of  $440 \text{ mAh g}^{-1}$  retained after 100 cycles at  $50 \text{ mA g}^{-1}$ . This work provides a new design of anode for high-performance Na-ion batteries.

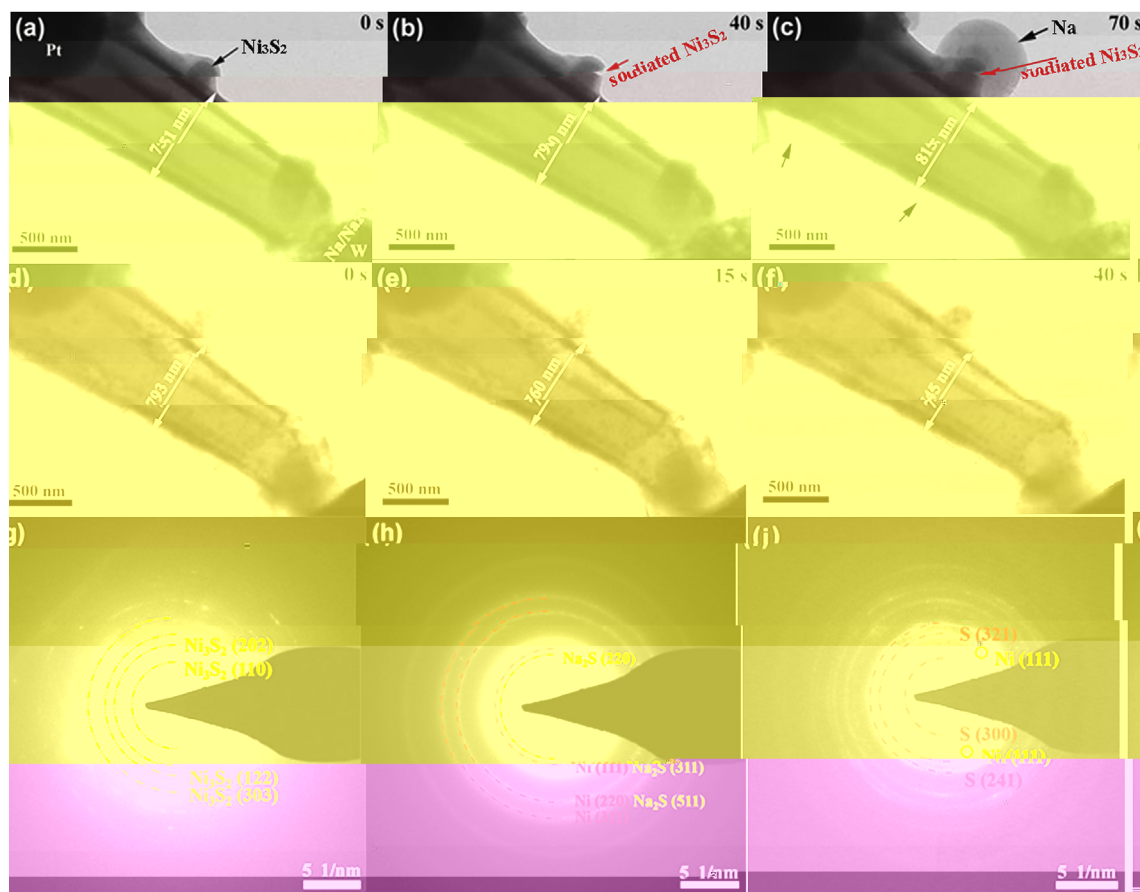


Fig. 6. Dynamic processes of (a–c) sodiation and (d–f) desodiation of a  $\text{Ni}_3\text{S}_2/\text{ACS}$  rod, and SAED patterns of the (g) pristine, (h) sodiated and (i) desodiated  $\text{Ni}_3\text{S}_2/\text{ACS}$ .

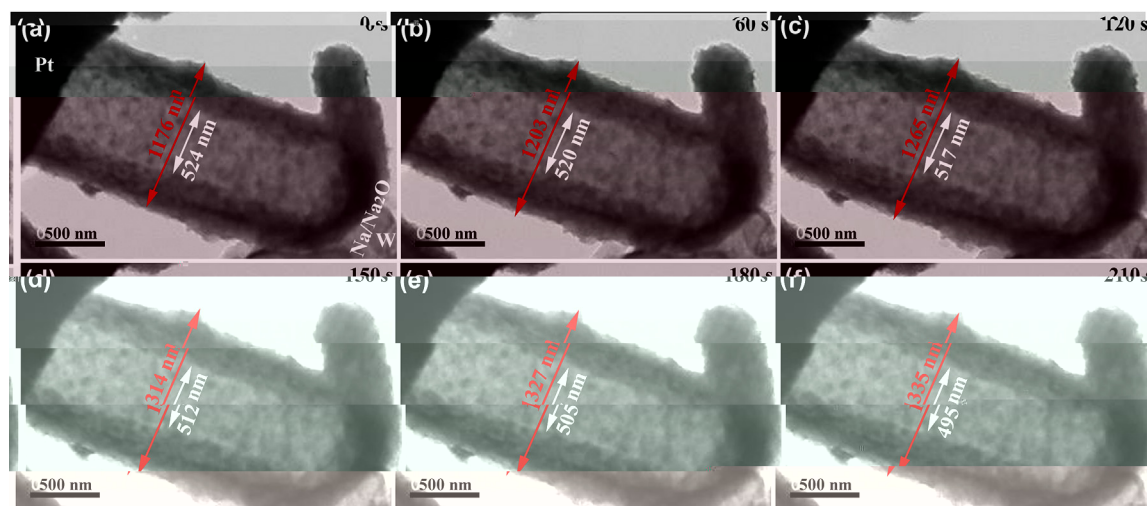


Fig. 7. Dynamic sodiation process of a thicker  $\text{Ni}_3\text{S}_2/\text{ACS}$  rod.

## Acknowledgements

This work was supported by the National Basic Research Program of China (2013CB934001), the National Natural Science Foundation of China (No. 51572238), Zhejiang Provincial Natural Science Foundation of China under Grant No. LY15E010004, Development and Application for Sodium Ion battery (2016GK4030), and Program for Innovative Research Team in

University of Ministry of Education of China (IRT13037). J.W. acknowledges the support of the Chinese 1000-Youth-Talent Plan.

## Appendix A. Supplementary data

Supplementary data related to this article can be found at <http://dx.doi.org/10.1016/j.mtener.2017.05.003>.

## References

- [1] U. Eberle, R. von Helmolt, Sustainable transportation based on electric vehicle concepts: a brief overview, *Energy Environ. Sci.* 3 (2010) 689–699.
- [2] V. Etacheri, R. Marom, R. Elazari, G. Salitra, D. Aurbach, Challenges in the development of advanced Li-ion batteries: a review, *Energy Environ. Sci.* 4 (2011) 3243–3262.
- [3] M.M. Thackeray, C. Wolverton, E.D. Isaacs, Electrical energy storage for transportation—approaching the limits of, and going beyond, lithium-ion batteries, *Energy Environ. Sci.* 5 (2012) 7854–7863.
- [4] J.B. Dunn, L. Gaines, J.C. Kelly, C. James, K.G. Gallagher, The significance of Li-ion batteries in electric vehicle life-cycle energy and emissions and recycling's role in its reduction, *Energy Environ. Sci.* 8 (2015) 158–168.
- [5] J.M. Tarascon, Is lithium the new gold? *Nat. Chem.* 2 (2012) 510, 510.
- [6] S.W. Kim, D.H. Seo, X.H. Ma, G. Ceder, K. Kang, Electrode materials for rechargeable sodium-ion batteries: potential alternatives to current lithium-ion batteries, *Adv. Energy Mater.* 2 (2012) 710–721.
- [7] M.D. Slater, D. Kim, E. Lee, C.S. Johnson, Sodium-ion batteries, *Adv. Funct. Mater.* 23 (2013) 947–958.
- [8] V. Palomares, P. Serras, I. Villaluenga, K.B. Hueso, J. Carretero González, T. Rojo, Na-ion batteries: recent advances and present challenges to become low cost energy storage systems, *Energy Environ. Sci.* 5 (2012) 5884–5901.
- [9] V. Palomares, M. Casas Cabanas, E. Castillo Martínez, M.H. Han, T. Rojo, Update on Na-based battery materials. A growing research path, *Energy Environ. Sci.* 6 (2013) 2312–2337.
- [10] N. Yabuuchi, K. Kubota, M. Dahbi, S. Komaba, Research development on sodium-ion batteries, *Chem. Rev.* 114 (2014) 11636–11682.
- [11] D. Kundu, E. Talaie, V. Duffort, L.F. Nazar, The emerging chemistry of sodium ion batteries for electrochemical energy storage, *Angew. Chem. Int. Ed.* 54 (2015) 3431–3448.
- [12] L.P. Wang, L.H. Yu, X. Wang, M. Srinivasan, Z.J. Xu, Recent developments in electrode materials for sodium-ion batteries, *J. Mater. Chem. A* 3 (2015) 9353–9378.
- [13] B. Dunn, H. Kamath, J.M. Tarascon, Electrical energy storage for the grid: a battery of choices, *Science* 334 (2011) 928–935.
- [14] M. Sawicki, L.L. Shaw, Advances and challenges of sodium ion batteries as post lithium ion batteries, *RSC Adv.* 5 (2015) 53129–53154.
- [15]